

A Cartesian method with second-order pressure resolution for incompressible flows with large density ratios

Michel Bergmann ^{1,‡}  and Lisl Weynans ^{2,‡,*}

¹ Memphis team, INRIA, Talence, France
University of Bordeaux, IMB, Talence, France
CNRS, IMB, Talence, France; michel.bergmann@inria.fr

² Carmen team, INRIA, Talence, France
University of Bordeaux, IMB, Talence, France
CNRS, IMB, Talence, France; lisl.weynans@math.u-bordeaux.fr

* Correspondence: lisl.weynans@math.u-bordeaux.fr

‡ These authors contributed equally to this work.

Abstract: An Eulerian method to numerically solve incompressible bifluid problems with high density ratio is presented. This method can be considered as an improvement of the Ghost-Fluid method, with the specificity of a sharp second-order numerical scheme for the spatial resolution of the discontinuous elliptic problem for the pressure. The Navier-Stokes equations are integrated in time with a fractional step method based on the Chorin scheme and discretized in space on a Cartesian mesh. The bi-fluid interface is implicitly represented using a level set function. The advantage of this method is its simplicity to implement in a standard mono-fluid Navier-Stokes solver while being more accurate and conservative than other simple classical bi-fluid methods. The numerical tests highlight the improvements obtained with this sharp method compared to the reference standard first-order methods.

Keywords: incompressible Navier-Stokes equations, projection method, finite differences, Cartesian grid, immersed interfaces, level-set, interface unknowns

1. Introduction

Bifluid problems are ubiquitous in nature and in many industrial applications like combustion in engines, water waves energy converters, and jet printers to only cite few. In such applications, the density ratio between the two fluids can be large, for instance the ratio is equal to 1000 between water and air. Accurate numerical modeling and numerical simulations of these kind of phenomena is then necessary, in particular to optimize such devices.

In this paper we are thus concerned with the numerical modeling of incompressible bi-fluid flows with large density ratios, like air and water, and by the accurate description of the phenomena occurring at their interface. We present a sharp Cartesian method for the simulation of incompressible flows with high density and viscosity ratios. This method is an extension of the second-order Cartesian method for elliptic problems with immersed interfaces developed in [1].

Cartesian grids are an attractive alternative to body fitted meshes. Indeed, they avoid complex mesh generation as well as mesh adaptation when unsteady interfaces are considered. Moreover, the numerical resolution of the governing equations can be simplified with an easy parallelization and the use of standard linear algebra libraries. Generally speaking, numerical schemes are easy to implement on a Cartesian mesh because a dimensional splitting is often possible. However, some numerical modeling is necessary near a complex interface that does not fit the background Cartesian grid. This is the case for fluid structure interface and moreover for bi-fluid interface where the properties of the flow are discontinuous. Indeed, applying naively a numerical scheme originally devised for a flow with constant or continuously varying density will lead to a non-consistent treatment of the interface. Most of the time, it will result in severe stability issues if the density ratio is large as highlighted in [2] and references therein. Therefore, as already mentioned, one has to devise specific numerical schemes at the vicinity of the interface. This region is called narrow band and is the set of numerical points that have at least one neighbor on the other side of the interface.

Citation: Bergmann, M.; Weynans, L. A Cartesian method with second-order pressure resolution for incompressible flows with large density ratios. *Preprints* 2021, 1, 0. <https://doi.org/>

Received:

Accepted:

Published:

Publisher's Note: MDPI stays neutral with regard to jurisdictional claims in published maps and institutional affiliations.

37 Conservative or non-conservative approaches can both be used to face this issue. Among
 38 the non-conservative approaches, one solution is to regularize the properties of the fluids in
 39 the vicinity of the interface, so that the density, viscosity, and their derivatives are continuous
 40 in the whole computational domain. This idea leads to the well known "Continuous Surface
 41 Force" (CSF) method [3], where the discontinuous quantities are smoothed near the interface,
 42 and in case of a fluid with surface tension, this surface tension is taken into account as a smooth
 43 volume force instead of a surface force. This method is widely used (see for instance [4] and
 44 [5]) because it offers a straightforward way to implement the presence of two fluids in an already
 45 existing mono-fluid Navier-Stokes code. However, the exact way that the regularization should
 46 be performed is not always clear, and spurious oscillations at the bi-fluid interface can appear due
 47 to errors in the pressure gradient computations. Another non-conservative method introduced
 48 by Kang, Fedkiw and Liu [6] after the CSF is the Ghost Fluid Method (GFM). It is based on
 49 a first-order method developed in [7] to solve an immersed interface elliptic problem, with a
 50 dimensional splitting making the method easy to implement. The resulting linear system is
 51 symmetric and has the same structure as the usual matrix to discretize a Poisson equation with
 52 variable coefficient on a Cartesian grid. This method has been used successfully in a lot of works,
 53 for instance [8] and [9]. One drawback is that the method is only first-order accurate near the
 54 interface [2] and a loss of conservativity of the momentum of each fluid near the interface can
 55 occur leading to erroneous velocities.

56 Non-conservative methods are often associated with a level-set representation of the inter-
 57 face [4] because the level-set method is itself intrinsically non-conservative at the discrete level,
 58 and convenient to use on a Cartesian grid.

59 The other family of methods is based on the conservative form of the Navier-Stokes equa-
 60 tions, where mass and momentum fluxes of each fluid are explicitly computed, see for instance
 61 [10], [11], [12], [13] and [2]. An explicit interface representation is necessary even if the interface
 62 do not coincide with grid points. Conservative methods are generally more stable than non-
 63 conservative methods. The price for this increased stability is an additional amount of numerical
 64 developments due to the interface reconstruction, which can be performed from informations
 65 carried by Lagrangian markers or by cell quantities such as volume fractions.

66 Another approach has been developed recently [14,15] to deal with large density ratio. In
 67 this approach, a fully second order method is obtained at the interface (for both velocity and
 68 pressure) with several physical boundary treatments, including velocity and traction boundary
 69 conditions.

70 In this paper we aim to preserve as much as possible the simplicity of the Ghost-Fluid
 71 Method of [6], avoiding an explicit identification of the volume fractions near the interface, while
 72 improving the accuracy and stability of the pressure computation. We thus propose a method,
 73 mainly based on the improvement of the Ghost-Fluid method, where the discontinuities across
 74 the interface are taken into account in a sharp way with a second-order scheme inspired from
 75 [1]. This second-order treatment improves the conservativity of the method, as it will be proved
 76 numerically in the section devoted to numerical validations.

77 After having described the governing equations for the incompressible bi-fluid flows that
 78 we consider (§2), the discretization of these equations in each fluid and at the interface are
 79 presented (§3-4). The second-order numerical resolution of the elliptic problem arising from
 80 the computation of the pressure is introduced (§5), and the overall is validated on several two-
 81 dimensional numerical test cases (§6).

82 2. Governing equations

83 2.1. Flow equations

84 We consider a rectangular domain Ω filled with two viscous incompressible fluids with
 85 different densities and viscosities. The subdomains Ω^- and Ω^+ corresponding to the two fluids
 86 are separated by an interface Γ as depicted in Figure 1.

87 In this work, these domains are implicitly defined with a scalar function ϕ , usually called
 88 the level-set function, see subsection 2.2, that takes different values in each subdomain with a
 89 fixed value on the interface. For instance we chose $\phi = 0$ on Γ , $\phi > 0$ in Ω^+ and $\phi < 0$ in Ω^- .

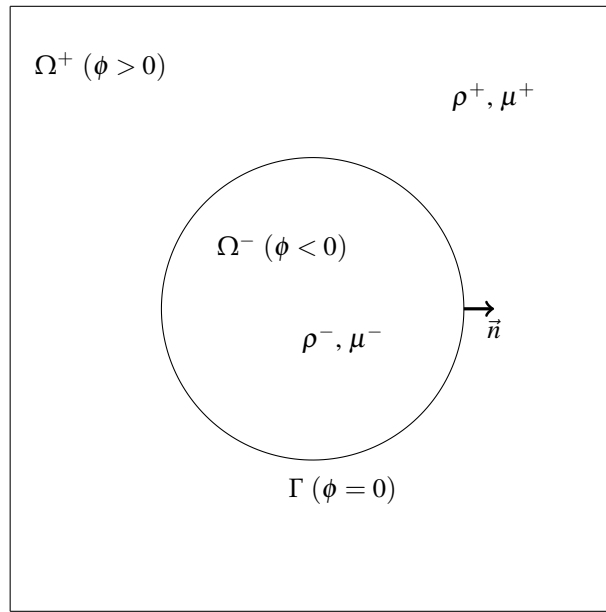


Figure 1. Sketch of the computational domain.

90 The unit normal to the interface is denoted \mathbf{n} and the unit tangent vector is denoted $\boldsymbol{\eta}$. The density
91 is denoted

$$\rho = \rho^- + H(\phi)(\rho^+ - \rho^-), \quad (1)$$

92 and the viscosity is denoted

$$\mu = \mu^- + H(\phi)(\mu^+ - \mu^-), \quad (2)$$

93 where H is the Heavyside function, *i.e.* $H(\phi) = 1$ if $\phi > 0$ and $H(\phi) = 0$ if $\phi < 0$. Finally,
94 the two-dimensional velocity vector is denoted $\mathbf{u} = (u, v)$.

95 The flow is modeled in the whole domain with the incompressible Navier-Stokes equations:

$$\begin{aligned} \rho(\mathbf{u}_t + (\mathbf{u} \cdot \nabla)\mathbf{u}) &= -\nabla p + \nabla \cdot \boldsymbol{\tau} + \rho \mathbf{g} - \sigma \kappa \nabla H, \\ \nabla \cdot \mathbf{u} &= 0, \end{aligned}$$

96 with \mathbf{g} the gravitational acceleration vector, $\boldsymbol{\tau}$ the viscous stress tensor:

$$\boldsymbol{\tau} = \mu(\nabla \mathbf{u} + \nabla \mathbf{u}^T), \quad (3)$$

97 and the term $\sigma \kappa \nabla H$ accounting for the surface tension effects, with σ the surface tension
98 itself and κ the local curvature of the interface between the fluids. This formulation of the bifluid
99 incompressible Navier-Stokes equations contains a singular term which is not trivial to handle.

100 Alternatively, the flow can also be modeled in each subdomain with the incompressible
101 Navier-Stokes equations:

$$\begin{aligned} \rho(\mathbf{u}_t + (\mathbf{u} \cdot \nabla)\mathbf{u}) &= -\nabla p + \nabla \cdot \boldsymbol{\tau} + \rho \mathbf{g}, \\ \nabla \cdot \mathbf{u} &= 0. \end{aligned}$$

102 The above equations are completed by jump conditions at the interface Γ between the
103 two fluids. In what follows jumps are defined by the notation $[\psi] = \psi^+ - \psi^-$. The first jump
104 conditions describe the balance between the normal stresses at the interface and the surface
105 tension σ , with κ the local curvature of the interface Γ ,

$$[p - 2\mu(\nabla u \cdot \mathbf{n}, \nabla v \cdot \mathbf{n}) \cdot \mathbf{n}] = \sigma \kappa, \quad (4)$$

$$[\mu(\nabla u \cdot \mathbf{n}, \nabla v \cdot \mathbf{n}) \cdot \boldsymbol{\eta} + (\nabla u \cdot \boldsymbol{\eta}, \nabla v \cdot \boldsymbol{\eta}) \cdot \mathbf{n}] = 0. \quad (5)$$

106 Others jump conditions can be derived from continuity properties across the interface. For
107 instance, for a viscous fluid the velocity field is continuous across the interface

$$[u] = 0, \quad (6)$$

$$[v] = 0. \quad (7)$$

108 Since the material derivative of (6)-(7) is zero, one can write

$$0 = \frac{\partial [u]}{\partial t} + (\mathbf{u} \cdot \nabla)[u] = \left[-\frac{\nabla p}{\rho} + \frac{\nabla \cdot \boldsymbol{\tau}}{\rho} + \mathbf{g} \right], \quad (8)$$

109 which leads to

$$\left[\frac{\nabla p}{\rho} \right] = \left[\frac{\nabla \cdot \boldsymbol{\tau}}{\rho} \right]. \quad (9)$$

110 The jump condition for the pressure p can be simplified. We differentiate the jump on the
111 velocity in the tangential direction:

$$\begin{aligned} \left[\frac{\partial u}{\partial \eta} \right] &= 0, \\ \left[\frac{\partial v}{\partial \eta} \right] &= 0. \end{aligned}$$

112 Moreover, because the velocity is divergent-free on each side of the interface,

$$0 = [\nabla \cdot \mathbf{u}] = [(\nabla u \cdot \mathbf{n}, \nabla v \cdot \mathbf{n}) \cdot \mathbf{n} + (\nabla u \cdot \boldsymbol{\eta}, \nabla v \cdot \boldsymbol{\eta}) \cdot \boldsymbol{\eta}]. \quad (10)$$

113 Combining the two last relationships, we obtain

$$[(\nabla u \cdot \mathbf{n}, \nabla v \cdot \mathbf{n}) \cdot \mathbf{n}] = 0. \quad (11)$$

114 Consequently

$$[p] = 2[\mu](\nabla u \cdot \mathbf{n}, \nabla v \cdot \mathbf{n}) \cdot \mathbf{n} + \sigma \kappa. \quad (12)$$

115 Finally, we will use equations (9) and (12) to compute the pressure jump at the interface.

116 2.2. Interface description

117 The interface between the two fluid subdomains is implicitly defined by a scalar function ϕ .
118 Local geometrical information on the function ϕ is needed to obtain an accurate discretization of
119 the interface. To this purpose we use the level set method, introduced by Osher and Sethian [16]
120 and described in [17], [18] and [19]. A common choice for the level-set function ϕ is the signed
121 distance function to the interface:

$$\phi(x) = \begin{cases} \text{dist}_\Gamma(x) & \text{if } x \in \Omega^+, \\ -\text{dist}_\Gamma(x) & \text{if } x \in \Omega^-, \\ 0 & \text{if } x \in \Gamma. \end{cases} \quad (13)$$

122 The zero isoline of ϕ thus represents implicitly the interface Γ immersed in the computational
123 domain.

124 We assume that the interface is smooth enough, so that the derivatives of the level-set
 125 function in the vicinity of the interface are well-defined. A useful property of the level-set
 126 function is a straightforward computation of its normal with the formula

$$\mathbf{n}(x) = \frac{\nabla\phi(x)}{|\nabla\phi(x)|}. \quad (14)$$

127 In the same way, the curvature of the interface can be computed with the formula

$$\kappa = \nabla \cdot \mathbf{n}. \quad (15)$$

128 We impose a curvature threshold $1/h$, with h the grid spacing, corresponding to the minimum
 129 size of a bubble for a given spatial discretization.

130 For a moving interface as it is usually the case for bi-fluid problems, the flow density and
 131 viscosity are updated with ϕ tracking the interface thanks to the transport equation

$$\phi_t + \hat{\mathbf{u}} \cdot \nabla\phi = 0, \quad (16)$$

132 where the velocity fields $\hat{\mathbf{u}}$ coincides with the flow velocity field \mathbf{u} on the interface Γ .
 133 Different choices for the value of $\hat{\mathbf{u}}$ in Ω^+ and Ω^- can be *a priori* used. A natural choice we
 134 have considered is $\hat{\mathbf{u}} = \mathbf{u}$ in the whole domain:

$$\phi_t + \mathbf{u} \cdot \nabla\phi = 0. \quad (17)$$

135 Another possible choice is the extension velocity introduced in [20].

136 3. Navier-Stokes monofluid solver and numerical method for interface evolution

137 The computational domain is discretized on a two-dimensional uniform Cartesian grid with
 138 a grid spacing $\Delta x = \Delta y = h$. However, the following approach stands for non uniform Cartesian
 139 meshes. The points on the Cartesian grid are defined as $M_{i,j} = (x_i, y_j)$. Similarly, we denote by
 140 u_{ij} the approximation of u at the point (x_i, y_j) . In what follows, all the unknowns are collocated
 141 in space on Cartesian meshes. An odd-even coupling can sometimes be observed when one uses
 142 collocated unknowns on a Cartesian grid. This problem can be fixed using some corrections such
 143 as [21,22]. However, in all the applications considered in this paper we have not observed any
 144 odd-even coupling.

145 In this section we present the numerical solver devised for monofluid incompressible Navier-
 146 Stokes equations that is used in each fluid when the interface is not taken into account. We also
 147 provide informations about the numerical methods used to compute the evolution of the level-set
 148 function.

149 3.1. Flow computation

150 We use a classical projection method [23,24] to solve the Navier-Stokes equations in each
 151 fluid outside the narrow band. In what follows, a non-incremental projection method is used, *i.e.*
 152 the guess value for the pressure in the prediction step is zero.

153 We thus compute successively:

$$\frac{\mathbf{u}^* - \mathbf{u}^n}{\Delta t} = -(\mathbf{u}^n \cdot \nabla)\mathbf{u}^n + \frac{1}{\rho}(\nabla \cdot \boldsymbol{\tau})^n + \mathbf{g} \quad (\text{prediction step}), \quad (18)$$

$$\frac{\mathbf{u}^{n+1} - \mathbf{u}^*}{\Delta t} = -\frac{\nabla p}{\rho} \quad (\text{correction step}). \quad (19)$$

154 The convective terms are computed with a fifth-order WENO scheme, and the viscous terms
 155 with an explicit second-order centered finite-difference scheme. The time integration is performed
 156 with a first-order explicit Euler scheme, which is consistent with the use of a non-incremental
 157 version of the projection scheme.

158 The pressure appearing in equation (19) is computed through the resolution of a Poisson
 159 equation in order to enforce the divergence-free condition. At each point in one subdomain, the
 160 following relationship is satisfied:

$$\nabla \cdot \left(\frac{1}{\rho} \nabla p \right) = \frac{\nabla \cdot \mathbf{u}^*}{\Delta t}. \quad (20)$$

161 We will provide additional details about the jump conditions that have to be satisfied across
 162 the interface for this problem in section 4. On the exterior boundary of the domain Ω , Neumann
 163 boundary conditions are satisfied:

$$\frac{\nabla p}{\rho} = \frac{\mathbf{u}^b - \mathbf{u}^*}{\Delta t}, \quad (21)$$

164 where \mathbf{u}^b is the value of the velocity to be imposed on the external boundaries.

165 We compute at each iteration an adaptive time step taking into account the restrictions due
 166 to convection, viscosity and surface tension. The convective time step restriction is given by

$$\Delta t \left(\frac{|u|_{\max}}{\Delta x} + \frac{|v|_{\max}}{\Delta y} \right) \leq 1. \quad (22)$$

167 with $|u|_{\max}$ and $|v|_{\max}$ the maximum magnitudes of the horizontal and vertical velocities.
 168 The viscous time step restriction is given by

$$\Delta t \left(\max \left(\frac{\mu^-}{\rho^-}, \frac{\mu^+}{\rho^+} \right) \left(\frac{2}{\Delta x^2} + \frac{2}{\Delta y^2} \right) \right) \leq 1 \quad (23)$$

169 We also apply a time step restriction associated with the surface tension evaluated only in
 170 the narrow band. This time step restriction is similar to the one in [6] and in [8], and is in this
 171 context usually the most restrictive:

$$\Delta t \sqrt{\frac{\sigma |\kappa|}{\min(\rho^+, \rho^-) \min(\Delta x^2, \Delta y^2)}} \leq 1. \quad (24)$$

172 Finally, at each time step, the overall algorithm is the following:

- 173 • Prediction: evaluate convective and diffusive fluxes and compute \mathbf{u}^* ,
- 174 • Interface evolution: convect the level-set with velocity \mathbf{u} and re-initialize if necessary,
- 175 • Construction and resolution of the linear system for the pressure,
- 176 • Correction step: update velocity with pressure gradient.

177 3.2. Numerical method for the level-set evolution

178 The computation of the level-set function should be performed very accurately when one
 179 deals with moving interfaces. Indeed, as the level-set method is not intrinsically conservative, a
 180 lack of accuracy in the computation of the level set evolution results often in a substantial loss of
 181 mass for one of the fluids. It can also increase the problem of transfer of momentum between
 182 both fluids and generate spurious velocity oscillations. Moreover, if one wants to compute the
 183 curvature of the interface from (15), the level-set function needs to be accurate enough (at least
 184 third-order) so that the finite difference formulas used to discretize (15) are consistent.

185 Unfortunately, the property of the signed distance function is usually lost when the interface
 186 evolves with the flow velocity. The norm of the level set gradient can be far from unity. These
 187 gradients variations of the level-set are harmful to the accuracy of the numerical evaluation
 188 of the normal to the interface and the curvature. To circumvent the problem, Sussman et al.
 189 [4] introduced a reinitialization algorithm to recover the signed distance function through the
 190 resolution of the eikonal equation

$$|\nabla \phi| = 1. \quad (25)$$

191 Several methods have been developed over the years to perform this reinitialization step,
 192 either by using a relaxation method and searching a stationary solution to a time dependent
 193 Hamilton-Jacobi equation [4] or using a Gauss-Seidel based method as in fast marching methods
 194 [25,26] or fast sweeping methods [27].

195 The usual level set strategy for an evolving interface is thus the following:

- 196 • Use a transport equation to update ϕ .
- 197 • From time to time, reinitialize ϕ with the signed distance function.

198 One of the most widespread option in the literature is to combine a fifth-order WENO
 199 scheme [28] with a RK3 scheme, for the transport and for the reinitialization through a relaxation
 200 equation. It provides a high-order yet stable resolution. But, although the reinitialization procedure
 201 performed with such a numerical scheme may improve mass conservation, it also introduces some
 202 error by slightly moving the interface as shown in [29]. For this reason, Russo and Smereka [29]
 203 introduced a subcell fix taking into account the interface location in the reinitialization procedure.
 204 This technique was extended to a higher order accuracy in [30] through the use of third-order
 205 ENO schemes near the interface.

206 Usually, this reinitialization steps are performed uniformly every each n iterations. A recent
 207 study [31] proposes a strategy to sample the reinitialization steps based on interface deformation
 208 criteria. This should also be coupled with the high-order decentered reinitialization scheme of
 209 [30] near the interface.

210 In what follows, we will use the classical option of the fifth-order WENO scheme for the
 211 spatial discretization. Since it is the most commonly used technique in the literature, it will allow
 212 to distinguish the effects of the new scheme for the pressure computation from the effects of the
 213 reinitialization technique.

214 4. Navier-Stokes solver near the interface

215 4.1. Notations

216 Let us introduce some definitions and notations. A grid point is defined to be irregular if at
 217 least one of its neighbors is on the other side of the interface, *i.e.* if the sign of ϕ changes between
 218 this point and at least one of its neighbors, see Figure 2. The set of irregular points is called the
 219 narrow band. All the other points are called regular grid points.

220 We define the interface point $I_{i,j,E} = (\tilde{x}_{i,j,E}, y_j)$ as the intersection of the interface Γ and
 221 the *East* segment $[M_{ij}M_{i+1j}]$, if it exists. Similarly, the interface points $I_{i,j,W} = (\tilde{x}_{i,j,W}, y_j)$,
 222 $I_{i,j,N} = (x_i, \tilde{y}_{i,j,N})$ and $I_{i,j,S} = (x_i, \tilde{y}_{i,j,S})$ are respectively defined as the intersection of the interface
 223 and the *West* $[M_{i-1j}M_{ij}]$, *North* $[M_{ij}M_{ij+1}]$ and *South* $[M_{ij-1}M_{ij}]$ segments. With this notation
 224 the same interface point can be described in two different ways

$$I_{i,j,S} = I_{i,j-1,N} \text{ or } I_{i,j,E} = I_{i+1,j,W}. \quad (26)$$

225 The set of interface points is denoted Γ_h , see Figure 2 for an illustration.

226 4.2. Modelling choices for the discontinuities across the interface

227 In this study, the values of the viscosity and the densities are discontinuous across the
 228 interface. Therefore, if the numerical scheme for solving incompressible Navier-Stokes equations
 229 described previously in subsection 3.1 was applied on the irregular grid points of the narrow band,
 230 the approximations of the following terms would not be consistent:

- 231 • prediction step: viscous terms,
- 232 • correction step: divergence of the predicted velocity, elliptic operator, gradient of the
 233 pressure.

234 This lack of consistency could eventually leads to stability problems.

235 The computation of the convective terms is not mentioned in the above enumeration because
 236 it is performed with a fifth-order WENO scheme, which provides automatically spatial adaptivity.
 237 Therefore, we assume that the gradients computed with the WENO scheme are decentered near
 238 the interface, and consequently, consistent. Moreover, the level-set function is classically evolved
 239 with such a scheme, because it is crucial to have a good accuracy in the computation of the

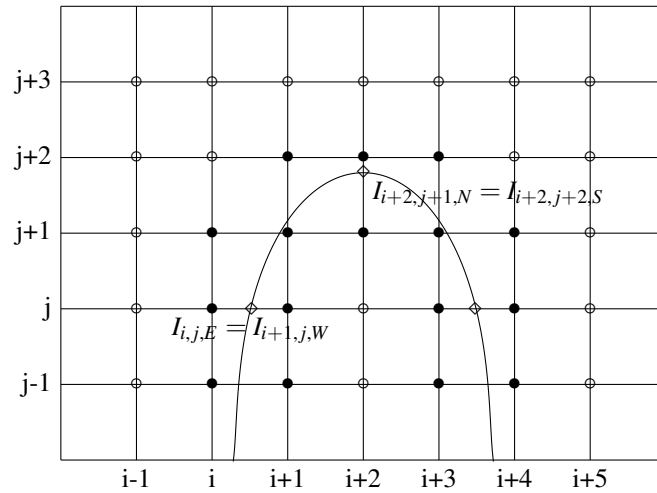


Figure 2. Example of geometrical configuration, with regular grid points (white circles), irregular points (black circles), and interface points (diamonds) with the two possible notations.

240 interface evolution. Therefore, it seems coherent to have the same numerical scheme for the
241 convection of the interface and the convection of the fluids.

242 In this work, we use two different strategies to handle the lack of consistency near the
243 interface, one for the viscous terms and another for the pressure computation. For the viscous
244 term in the prediction step, we follow a continuous approach and regularize the quantities used
245 for the computation of the viscous terms. It has been proven in [32] and [33] that this continuous
246 approach provides correct accuracy for high Reynolds numbers flows. It has also been used
247 successfully in [2] and [3]. A sharp approach for the viscous terms could probably improve the
248 accuracy of the simulations. However, the complexity of the computations would be increased
249 due to the treatment of the jump conditions for the viscous terms (5) implying derivatives of the
250 velocity components in both normal and tangential directions. Moreover, if one needs to use an
251 implicit treatment of the viscous terms, such a sharp treatment would become more complex to
252 handle.

253 The discretization of the prediction step becomes:

$$\frac{\mathbf{u}^* - \mathbf{u}^n}{\Delta t} = -(\mathbf{u}^n \cdot \nabla) \mathbf{u}^n + \frac{1}{\bar{\rho}} \left(\nabla \cdot \tilde{\mu} (\nabla \mathbf{u} + \nabla \mathbf{u}^T) \right)^n + \mathbf{g}. \quad (27)$$

254 In practice the viscosity and the inverse of the density were regularized by a discrete
255 convolution [2]:

$$\begin{aligned} 16 \tilde{\mu}_{i,j} &= 4\mu_{i,j} + 2\mu_{i+1,j} + 2\mu_{i-1,j} + 2\mu_{i,j+1} + 2\mu_{i,j-1} \\ &\quad + \mu_{i+1,j+1} + \mu_{i+1,j-1} + \mu_{i-1,j+1} + \mu_{i-1,j-1}, \\ \frac{16}{\tilde{\rho}_{i,j}} &= \frac{4}{\rho_{i,j}} + \frac{2}{\rho_{i+1,j}} + \frac{2}{\rho_{i-1,j}} + \frac{2}{\rho_{i,j+1}} + \frac{2}{\rho_{i,j-1}} \\ &\quad + \frac{1}{\rho_{i+1,j+1}} + \frac{1}{\rho_{i+1,j-1}} + \frac{1}{\rho_{i-1,j+1}} + \frac{1}{\rho_{i-1,j-1}}. \end{aligned}$$

256 Then we discretize the viscous terms with a classical second-order centered scheme as in
257 subsection 3.1.

258 In the correction step, according to the jump conditions (4) - (12) presented in section 2, the
259 pressure satisfies an elliptic problem with discontinuous values of the solution and its derivative
260 across the interface:

$$\begin{aligned}\nabla \cdot \left(\frac{1}{\rho} \nabla p \right) &= \frac{\nabla \cdot \mathbf{u}^*}{\Delta t} \text{ in } \Omega^+ \cup \Omega^-, \\ [p] &= \sigma \kappa + 2[\mu] (u_n, v_n) \cdot \mathbf{n} \text{ on } \Gamma, \\ \left[\frac{\nabla p}{\rho} \right] &= \left[\frac{\nabla \cdot \boldsymbol{\tau}}{\rho} \right] \text{ on } \Gamma.\end{aligned}$$

261 Because the viscous terms in the prediction step are handled with a regularization approach,
262 we have $[\mu] = 0$ and $\left[\frac{\nabla \cdot \boldsymbol{\tau}}{\rho} \right] = 0$. Therefore, the pressure computed for the correction step satisfies
263 rather:

$$\nabla \cdot \left(\frac{1}{\rho} \nabla p \right) = \frac{\nabla \cdot \mathbf{u}^*}{\Delta t} \text{ in } \Omega^+ \cup \Omega^-, \quad (28)$$

$$[p] = \sigma \kappa \text{ on } \Gamma, \quad (29)$$

$$\left[\frac{\nabla p}{\rho} \right] = 0 \text{ on } \Gamma. \quad (30)$$

264 The details of the resolution of this elliptic problem will be provided in section 5. Let us
265 remark however that as the values of p are discontinuous across the interface, two values of p
266 will be created at each point of the interface considered in the numerical scheme.

267 4.3. Gradient and divergence for correction step

268 The predicted velocity \mathbf{u}^* obtained after the prediction step (18) is defined only on grid
269 points. We need to compute the divergence of this predicted velocity in order to solve the elliptic
270 equation (20). However, since the two fluids have different properties across the interface and the
271 derivatives of the velocity are not necessarily continuous, we need to use a decentered stencil on
272 each side of the interface. Consequently, we have to compute two values for \mathbf{u}^* on each interface
273 point, one for each side of the interface. In practice, as jump conditions for \mathbf{u}^* are not available,
274 we perform simply linear extrapolations from the grid values on the interface points. Then, to
275 compute the divergence of \mathbf{u}^* on an irregular grid point $M_{i,j}$, we use a standard five point stencil,
276 see Figure 3. Formally this is equivalent to a standard first-order decentered scheme.

277 More precisely, we denote \mathbf{u}_S^* the value of the predicted velocity \mathbf{u}^* on the nearest point
278 to $M_{i,j}$ in the south direction (possibly an interface point), with coordinates (x_S, y_S) . Similarly,
279 we define \mathbf{u}_N^* , \mathbf{u}_W^* and \mathbf{u}_E^* and the associated coordinates (x_N, y_N) , (x_W, y_W) and (x_E, y_E) . The
280 discretization reads

$$(\nabla \cdot \mathbf{u}^*)_{i,j} = \frac{u_E^* - u_W^*}{x_E - x_W} + \frac{v_N^* - v_S^*}{y_N - y_S}.$$

281 Similarly, in order to keep a consistent discretization, the gradient of the pressure p appearing
282 in equation (19) is also computed with an adapted decentered stencil near the interface, see Figure
283 3. More precisely, with the same notations S , N , W and E , as before, the discretization reads

$$(\nabla p)_{i,j} = \begin{pmatrix} \frac{p_E - p_W}{x_E - x_W} \\ \frac{p_N - p_S}{y_N - y_S} \end{pmatrix}. \quad (31)$$

284 If one of the discretization point is an interface point, we consider the value of the pressure
285 on this point corresponding to the same subdomain than point $M_{i,j}$. Indeed we recall that, since the
286 pressure is discontinuous across the interface, two pressure unknowns (one for each subdomain)
287 are computed at an interface point. If no interface point is involved, the numerical scheme reduces
288 to the classical second-order central finite differences scheme.

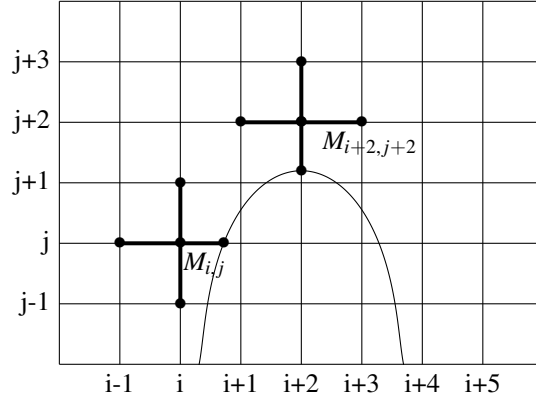


Figure 3. Example of geometrical configuration, with points involved in the discretization of the divergence of the predicted velocity and pressure gradient at grid points $M_{i,j}$ and $M_{i+2,j+2}$ in black.

289 5. Numerical resolution of elliptic problems with immersed interfaces

290 The elliptic problem with discontinuous values across an interface (28) - (30) is solved with
 291 the second-order method developed in [1]. The interface points are used to impose the jump
 292 conditions across the interface in the numerical scheme. Since the pressure is discontinuous
 293 across the interface, two unknowns are created, one for each side of the interface. The accuracy
 294 of this method is based on the use of unknowns located at the interface. The size of this linear
 295 system is thus augmented with two unknowns for each interface point. These interface unknowns
 296 are used to discretize the flux jump conditions and the elliptic operator accurately enough to
 297 get a second-order convergence in maximum norm. Actually, to this purpose, near the interface
 298 the elliptic operator needs to be discretized with a first-order truncation error, and the fluxes
 299 with a second-order truncation error. For a visual explanation of the discretization we refer to
 300 Figure 4. The advantage of using this method, compared to the reference work of [6] is that
 301 the jump conditions in the correction step are solved with second-order accuracy instead of
 302 first-order. The drawback is that the linear system is not symmetric anymore and it is solved with
 303 the preconditioned GMRES method.

304 5.1. Discrete elliptic operator

305 We use a standard five-point stencil including the grid point $M_{i,j}$ and its nearest neighbors in
 306 each direction: interface or grid points. More precisely, we denote p_S the value of the solution
 307 on the nearest point in the south direction, with coordinates (x_S, y_S) . Similarly, we define p_N ,
 308 p_W and p_E and the associated coordinates (x_N, y_N) , (x_W, y_W) and (x_E, y_E) . Since the density is
 309 piecewise constant, the discretization reads

$$\left(\nabla \cdot \left(\frac{1}{\rho^\pm} \nabla p \right) \right)_{i,j} = \frac{1}{\rho^\pm} \Delta p = \frac{1}{\rho^\pm} \frac{\frac{p_E - p_{ij}}{x_E - x_i} - \frac{p_{ij} - p_W}{x_i - x_W}}{\frac{x_E - x_W}{2}} + \frac{1}{\rho^\pm} \frac{\frac{p_N - p_{ij}}{y_N - y_j} - \frac{p_{ij} - p_S}{y_j - y_S}}{\frac{y_N - y_S}{2}}, \quad (32)$$

310 where ρ^\pm stands for ρ^+ or ρ^- .

311 5.2. Discrete flux transmission conditions

312 As written before, at each interface point we create two additional unknowns, called interface
 313 unknowns. We denote them by $p_{i,j,\gamma}^\pm$ with $\gamma = E, W, N$ or S . The interface unknowns carry the
 314 values of pressure on each side of the interface.

315 Contrarily to [1], we do not have a jump condition on the normal derivative, but on the
 316 whole gradient, as expressed in formula (30). To obtain the same number of equations and
 317 unknowns we have to chose in which direction we want to project this gradient equality. As we
 318 use a Cartesian grid, it is easier to discretize the x - and y -derivatives than derivatives in other

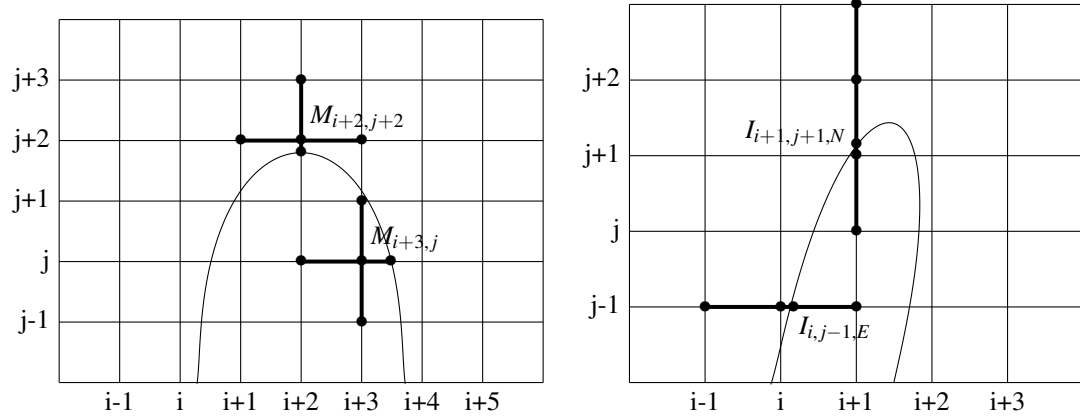


Figure 4. Left: points involved in the discretization of the elliptic operator at grid nodes $M_{i+2,j+2}$ and $M_{i+3,j}$ in black, right: Example of stencils for the discretization of jump conditions. Points involved in the discretization of the x-derivative of the pressure at interface point $I_{i,j-1,E}$ and of the y-derivative of the pressure at interface point $I_{i+1,j+1,N}$ in black. For $I_{i,j-1,E}$ both derivatives are expressed with second-order accuracy while for $I_{i+1,j+1,N}$ the left derivative is expressed with second-order and the right derivative with first-order accuracy.

319 directions. Consequently, we discretize the following jump conditions at each interface point $I_{i,j,\gamma}$,
 320 with $\gamma = N, S, W, E$.

$$p_{i,j,\gamma}^+ - p_{i,j,\gamma}^- = \sigma \kappa_{i,j,\gamma}, \quad (33)$$

$$\frac{1}{\rho^+} (\partial_x p^+)_{i,j,\gamma} - \frac{1}{\rho^-} (\partial_x p^-)_{i,j,\gamma} = 0 \text{ if } \gamma = E, W. \quad (34)$$

$$\frac{1}{\rho^+} (\partial_y p^+)_{i,j,\gamma} - \frac{1}{\rho^-} (\partial_y p^-)_{i,j,\gamma} = 0 \text{ if } \gamma = N, S. \quad (35)$$

321 We want the truncation error of the discretization of flux equality (34-35) to be second-order
 322 accurate in order to solve the problem with a second-order accuracy. A possible configuration
 323 of the interface is illustrated in Figure 4. In the x-direction, it is straightforward to compute a
 324 second-order approximation of the x-derivative with three *a priori* non equidistant points. For
 325 example we approximate the flux on the left side of interface point $I_{i,j,E}$, if it exists, with the
 326 values of p on the points $M_{i-1,j}$, $M_{i,j}$ and $I_{i,j,E}$ with the formula:

$$(\partial_x p^\pm)_{i,j,E} \approx \frac{(p_{i-1,j} - p_{i,j,E}^\pm)(x_i - \tilde{x}_{i,j,E})}{\Delta x(x_{i-1} - \tilde{x}_{i,j,E})} - \frac{(p_{i,j} - p_{i,j,E}^\pm)(x_{i-1} - \tilde{x}_{i,j,E})}{\Delta x(x_i - \tilde{x}_{i,j,E})}. \quad (36)$$

327 The right x-derivative is approximated in the same way.

$$(\partial_x p^\pm)_{i,j,E} \approx -\frac{(p_{i+2,j} - p_{i,j,E}^\pm)(x_{i+1} - \tilde{x}_{i,j,E})}{\Delta x(x_{i+2} - \tilde{x}_{i,j,E})} + \frac{(p_{i+1,j} - p_{i,j,E}^\pm)(x_{i+2} - \tilde{x}_{i,j,E})}{\Delta x(x_{i+1} - \tilde{x}_{i,j,E})}. \quad (37)$$

328 The same discretization holds for the y-derivative. The formulas (36) and (37) are consistent
 329 if both grid points involved in the formula, for instance $M_{i-1,j}$ and $M_{i,j}$, belong to the same
 330 domain. If on one side of the interface the two closest grid points aligned with the intersection
 331 point do not belong to the same subdomain, then the second-order discretization is not possible
 332 anymore. In this case, we use a first-order discretization involving only two points: the interface
 333 point and the closest grid point on the same side of the interface. Such a case is illustrated on
 334 Figure 4. In fact, this first-order discretization is equivalent to the ghost-fluid method [6].

335 Let us notice that, because we use a dimensional splitting for the jump conditions across the
 336 interface, it is quite straightforward to eliminate the interface unknowns from the linear system.
 337 We simply inject expressions (36) and (37) in the jump condition (34), and use the resulting
 338 equality to express $p_{i,j,E}^\pm$ as a function of $p_{i-1,j}$, $p_{i,j}$, $p_{i+1,j}$ and $p_{i+2,j}$. This expression for $p_{i,j,E}^\pm$
 339 can then be used in the discretization of the elliptic operator (32).

340 The local curvature $\kappa_{i,j,\gamma}$ at the interface point $I_{i,j,\gamma}$ is computed in the following way. We
 341 first compute on all irregular grid points the value

$$\kappa = \frac{\phi_x^2 \phi_{yy} + \phi_y^2 \phi_{xx} - 2\phi_x \phi_y \phi_{xy}}{(\phi_x^2 + \phi_y^2)^{3/2}} \quad (38)$$

342 with centered second-order finite-difference formulas. Then we perform a one-dimensional
 343 linear interpolation of these values on the interface points.

344 6. Numerical results and validations

345 This section is devoted to the numerical simulations and validations.

346 After having studied the well balanced behaviour of the proposed approach, *i.e.* the capacity
 347 of the method to preserve equilibria state for a bubble, in §6.1, we will perform a quantitative
 348 validation for the well known dam break problem §6.2. We then present other numerical simula-
 349 tions for the rising of bubbles with different sizes that can qualitatively been compared to some
 350 reference results §6.3.

351 6.1. Equilibria preservation for a bubble: the parasitic oscillations

352 This first test case aims to assess the influence of the interface curvature error on the stability
 353 of the numerical scheme. A bubble is located at the center of the computational domain in §6.1.1
 354 and §6.1.2. Due to Laplace law and the concavity of the interface, the pressure inside the bubble
 355 is larger than the pressure outside. If the curvature of the interface is computed numerically, the
 356 errors due to the numerical approximation in the right-hand side of equation (33) cause small
 357 errors in the resolution of the pressure equation and the system is thus not well balanced. These
 358 errors create artificial values of the velocity near the interface which should theoretically be
 359 zero. These artificial velocities are often called parasitic currents. The amplitude of the parasitic
 360 currents is an indication of the stability and the accuracy of the numerical method, and especially
 361 of the pressure computational step. Indeed, they are the only source of numerical errors.

362 In what follows several comparisons with other references methods, the Ghost Fluid and
 363 the CSF methods in §6.1.1 and the Volume Of Fluid method in §6.1.2, are presented on slightly
 364 different test cases.

365 6.1.1. Comparison with the Ghost Fluid and the CSF methods

366 We use the same parameters as in [8], where a Ghost-Fluid and a CSF method were
 367 implemented. The amplitude of the parasitic currents, compared to the results in [8], are reported
 368 in Table 1. The L^∞ and L^2 norms are computed over the whole domain Ω . The initial configuration
 369 is described in Figure 5. As it can be observed, the amplitude of the parasitic currents generated by
 370 our method is several orders of magnitude smaller than those of the CSF method, and significantly
 371 lower than those of the Ghost-Fluid method when the grid is refined.

$$\left\{ \begin{array}{l} L = 2 \text{ cm}, \\ R = 1 \text{ cm}, \\ \rho_{int} = 1000 \text{ kg.m}^{-3}, \\ \mu_{int} = 10^{-3} \text{ Pa.s}, \\ \rho_{ext} = 1 \text{ kg.m}^{-3}, \\ \mu_{ext} = 10^{-5} \text{ Pa.s}, \\ \sigma = 0.1 \text{ N.m}^{-1} \end{array} \right. \quad (39)$$

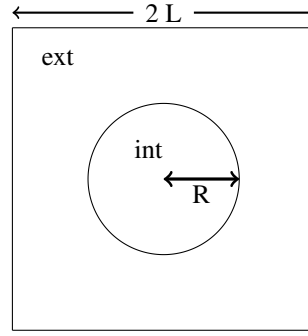


Figure 5. Test case of the static bubble with parasitic oscillations.

Table 1. Comparison between the new method and the numerical results obtained in [8] for the ghost-fluid method and the CSF method for parasitic oscillations, at time $t = 1$.

N	Ghost Fluid method		CSF		New method	
	L^∞ error	L^2 error	L^∞ error	L^2 error	L^∞ error	L^2 error
16	8.08×10^{-3}	1.88×10^{-3}	3.55×10^{-2}	1.94×10^{-2}	5.21×10^{-3}	7.31×10^{-5}
32	3.42×10^{-4}	7.50×10^{-5}	3.12×10^{-2}	1.18×10^{-2}	9.26×10^{-5}	1.42×10^{-6}
64	5.13×10^{-5}	7.97×10^{-6}	2.12×10^{-2}	5.44×10^{-3}	1.36×10^{-5}	1.47×10^{-7}
128	2.79×10^{-5}	4.74×10^{-6}	6.44×10^{-3}	1.38×10^{-3}	2.22×10^{-6}	1.92×10^{-8}

372 6.1.2. Comparison with a Volume of Fluid method

373 We now compare the behavior of our method to the Volume of Fluid method developed in
 374 [12]. The density and viscosity ratio are both chosen to be one for this test-case. The coefficient
 375 σ is chosen so as to obtain an Ohnesorge number $Oh = \frac{\mu}{\sqrt{\sigma \rho D}}$ satisfying $Oh^2 = \frac{1}{12000}$. The
 376 maximum velocity is computed for varying grids at non-dimensional time $t^* = \frac{t}{T} = 250$, with
 377 $T = \frac{D\mu}{\sigma}$.

$$\left\{ \begin{array}{l} L = 1.25 \text{ m,} \\ R = 1 \text{ m,} \\ \rho_{int} = 1 \text{ kg.m}^{-3}, \\ \mu_{int} = 10^{-3} \text{ Pa.s,} \\ \rho_{ext} = 1 \text{ kg.m}^{-3}, \\ \mu_{ext} = 10^{-3} \text{ Pa.s,} \\ \sigma = 0.00012 \text{ N.m}^{-1} \end{array} \right. \quad (40)$$

378 A comparison between our method and the Volume of Fluid method is presented in Table
 379 2. The new method provides a better accuracy than the Volume of Fluid method for the coarsest
 380 grid. As expected, the Volume of Fluid method outperforms our new approach for finer meshes
 381 due to more sophisticated schemes near the interface. Nonetheless, Table 2 show a second-order
 382 accuracy for our new method.

Table 2. Numerical results for parasitic oscillations at non-dimensional time $t^* = 250$ for [12] and our method.

Δx	error L^∞ for [12]	error L^∞ for our method
2.5/16	7.3×10^{-4}	7.48×10^{-5}
2.5/32	4.5×10^{-6}	4.7×10^{-6}
2.5/64	5.5×10^{-8}	1.26×10^{-6}

383 6.2. Collapse of a water column: the dam break problem

384 This test case is studied in [2] and [34], and based on experiments conducted in [35]. The
 385 initial configuration is a water column at rest in air. The initial height and width of the column
 386 are both 5.715 cm. The domain size is 40 cm×10 cm. The physical constants are the same than
 387 for the rising bubble (§6.1.1). For more details, we refer the reader to [2]. We present in Figure
 388 6 the interface evolution at non-dimensional times $T = t\sqrt{g/H} = 0, 1, 2, 3, 4$, with H the initial
 height of the water column. The computations are performed with 256×64 points.

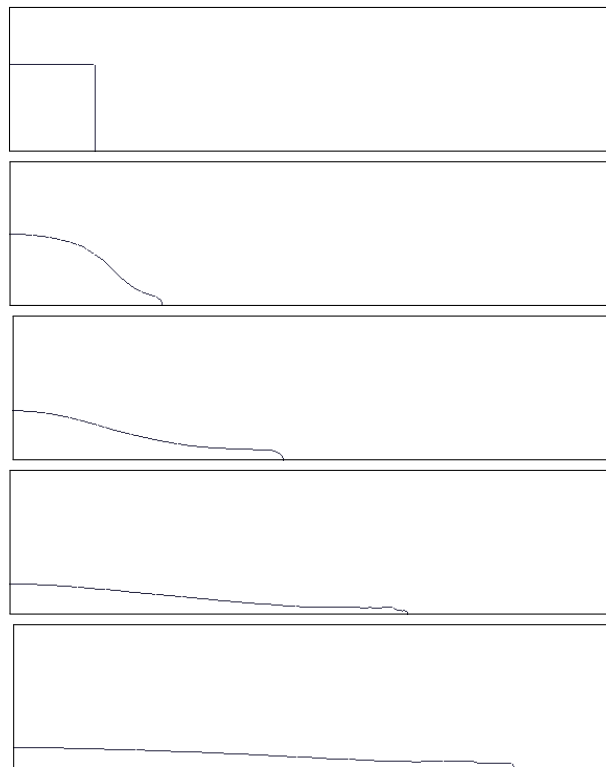


Figure 6. Evolution of the interface for the dam break problem at non-dimensional times $T = t\sqrt{g/H} = 0, 1, 2, 3, 4$.

389

390 Figure 7 present the temporal evolution of the water front, compared to the experimental
 391 results [35], to results with the Ghost-Fluid method used for pressure resolution, and to the
 392 conservative method of Raessi and Pitsch [2]. We observe that the front propagation is in
 393 agreements with the experimental results and the results of the conservative method [2]. It means
 394 that, though the method is not strictly conservative, the numerical errors due to momentum
 395 transfer across the interface are not large enough to slow down the propagation of the front. It is
 396 not the case for instance for the Ghost-Fluid method, as it can be noticed in Figure 7 and has been
 397 reported in [2].

398 6.3. Rising of air bubble in water

399 We study the evolution of fluid bubbles rising in a heavier fluid, and compare our results to
 400 several methods in the literature. The initial configuration is described in Figure 8.

401 6.3.1. Comparison with the Ghost-Fluid method

402 We consider air bubbles rising in water, as in the test case proposed for the Ghost-Fluid
 403 method in [6]. The value of the physical parameters are

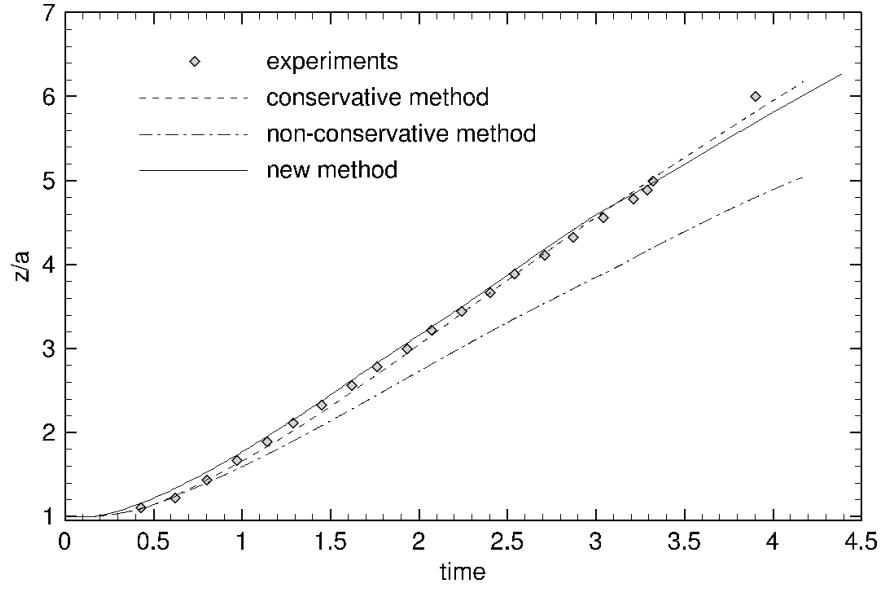


Figure 7. Evolution of the front of propagation: comparison between experimental data and several numerical methods: the Ghost Fluid method (non-conservative method), the conservative method of Raessi and Pitsch and our new method, The dimensionless location of the front $\frac{z}{a}$ is plotted as a function of the dimensionless time $T = t\sqrt{g/H}$.

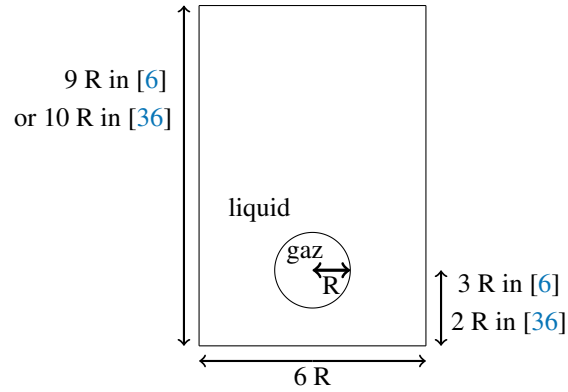


Figure 8. Initial fluid domain for the test case of the rising bubble in water in the references [6] and [36]

$$\left\{ \begin{array}{l} R = 1/300 m \text{ (small bubble)} \\ R = 1/3m \text{ (large bubble)} \\ \rho_{water} = 1000 \text{ kg/m}^3, \\ \mu_{water} = 1.137 \times 10^{-3} \text{ kg/ms}, \\ \rho_{air} = 1.226 \text{ kg/m}^3, \\ \mu_{air} = 1.78 \times 10^{-5} \text{ kg/ms}, \\ \sigma = 0.0728 \text{ kg/s}^2, \\ g = -9.8m/s^2. \end{array} \right. \quad (41)$$

404 We consider two cases: a small bubble with $R = 1/300m$ and a large one $R = 1/3m$. In
 405 the first case, the surface tension plays an important role in the evolution of the interface because
 406 of the high bubble curvature. In the second case, the surface tension has less influence, and larger
 407 deformations occur. The interface of the small bubble and the vorticity values are plotted at times
 408 $t = 0., 0.02, 0.035, 0.05$ in Figure 9. The interface of the large bubble and the vorticity values are
 409 plotted at times $t = 0., 0.2, 0.35, 0.5$ in Figure 10. Our numerical results are in good agreements
 410 with [6].

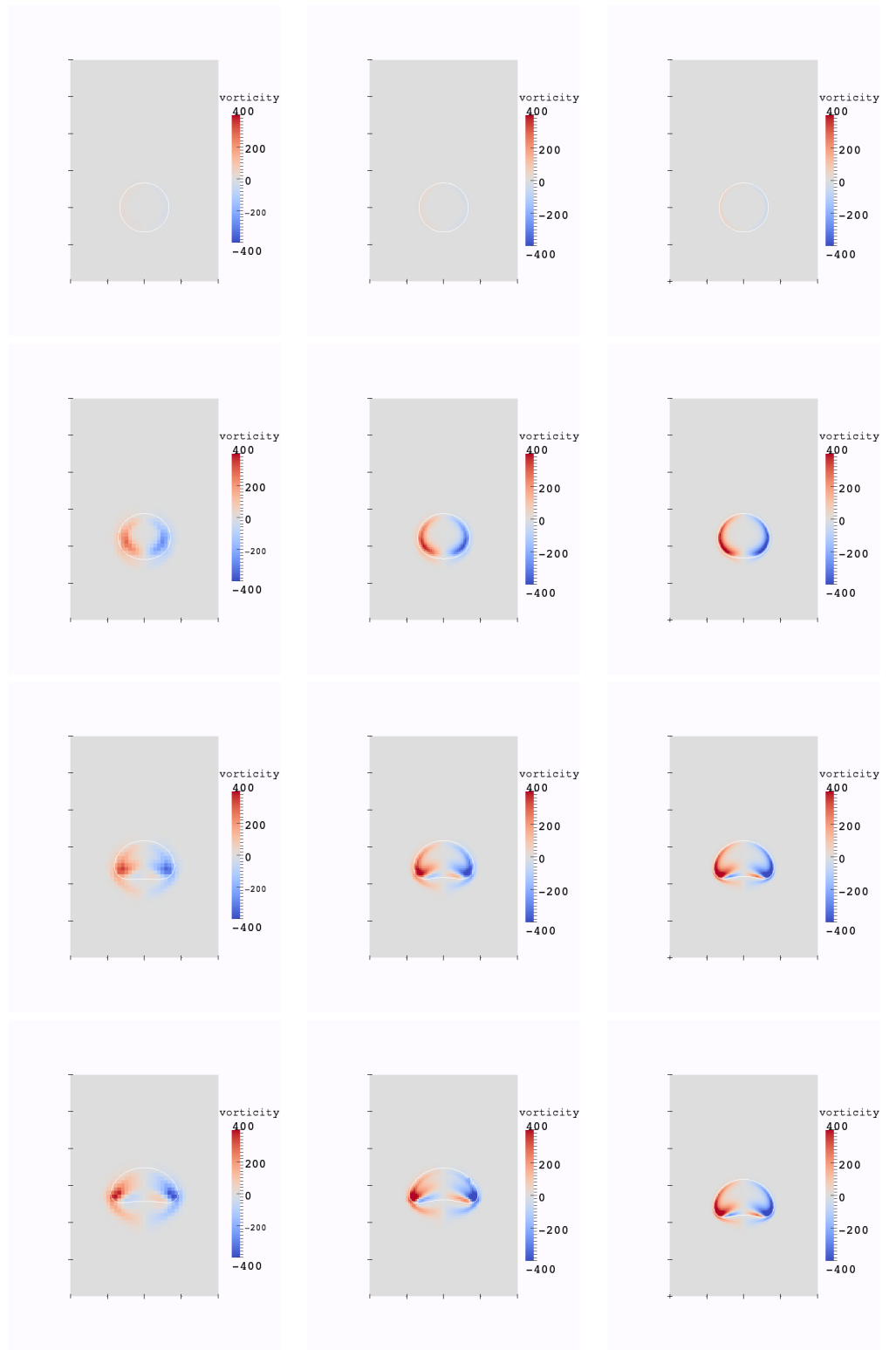


Figure 9. Evolution of the interface and vorticity values for the small bubble test case, at times 0.,0.02,0.035, 0.05, resolution 40×60 (left), 80×120 (middle) and 160×240 (right).

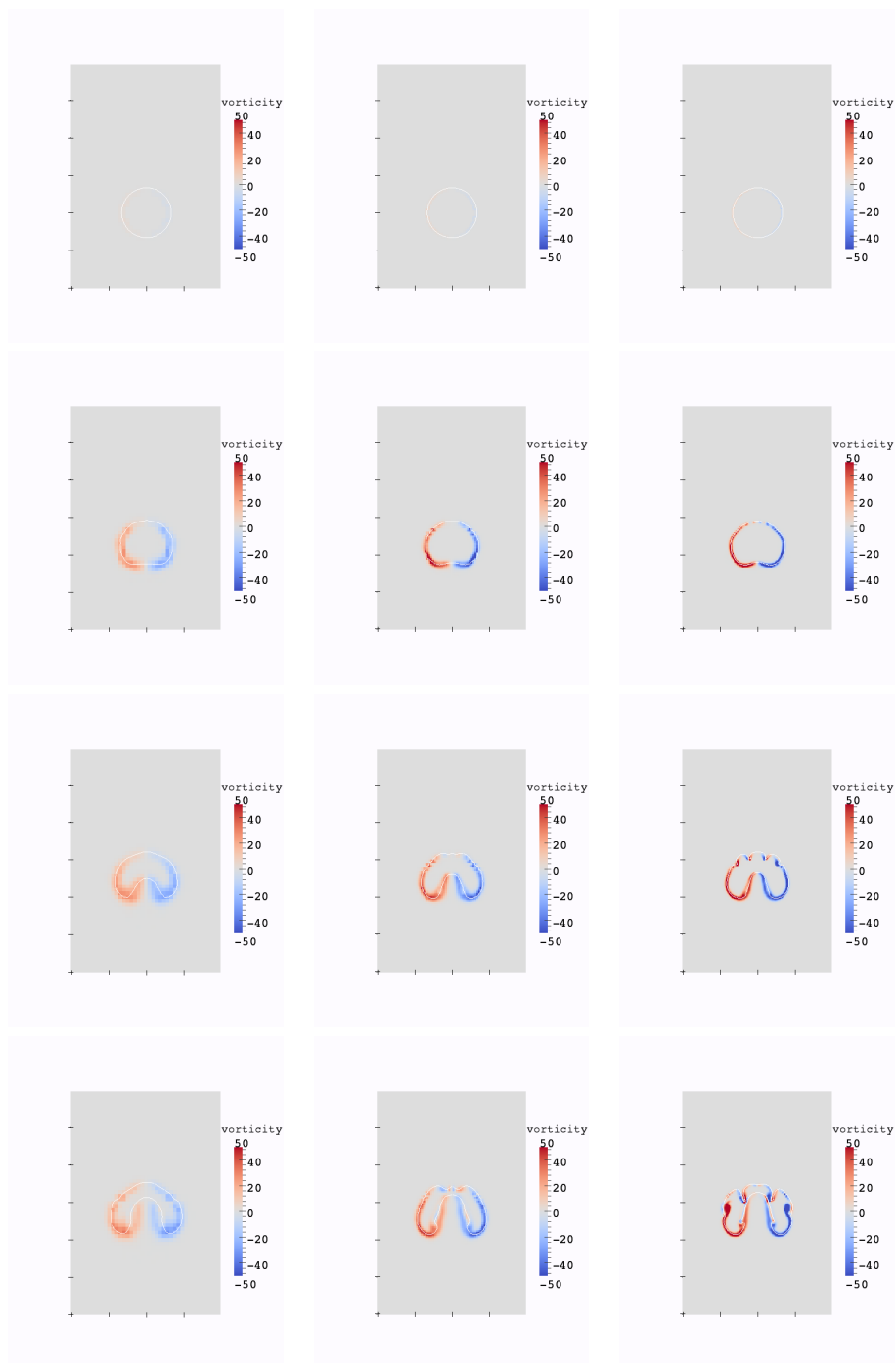


Figure 10. Evolution of the interface and vorticity values for the large bubble test case, at times 0,0.2,0.35, 0.5, resolution 40×60 (left), 80×120 (middle) and 160×240 (right).

411 6.3.2. Comparison with SPH and the level-set method

412 This test case is taken from [36], and inspired from a test case presented in [4]. It gives us the
 413 opportunity to compare our method to another class of methods, based on the SPH formulation.
 414 The initial configuration is described on Figure 8. The values of the physical parameters are

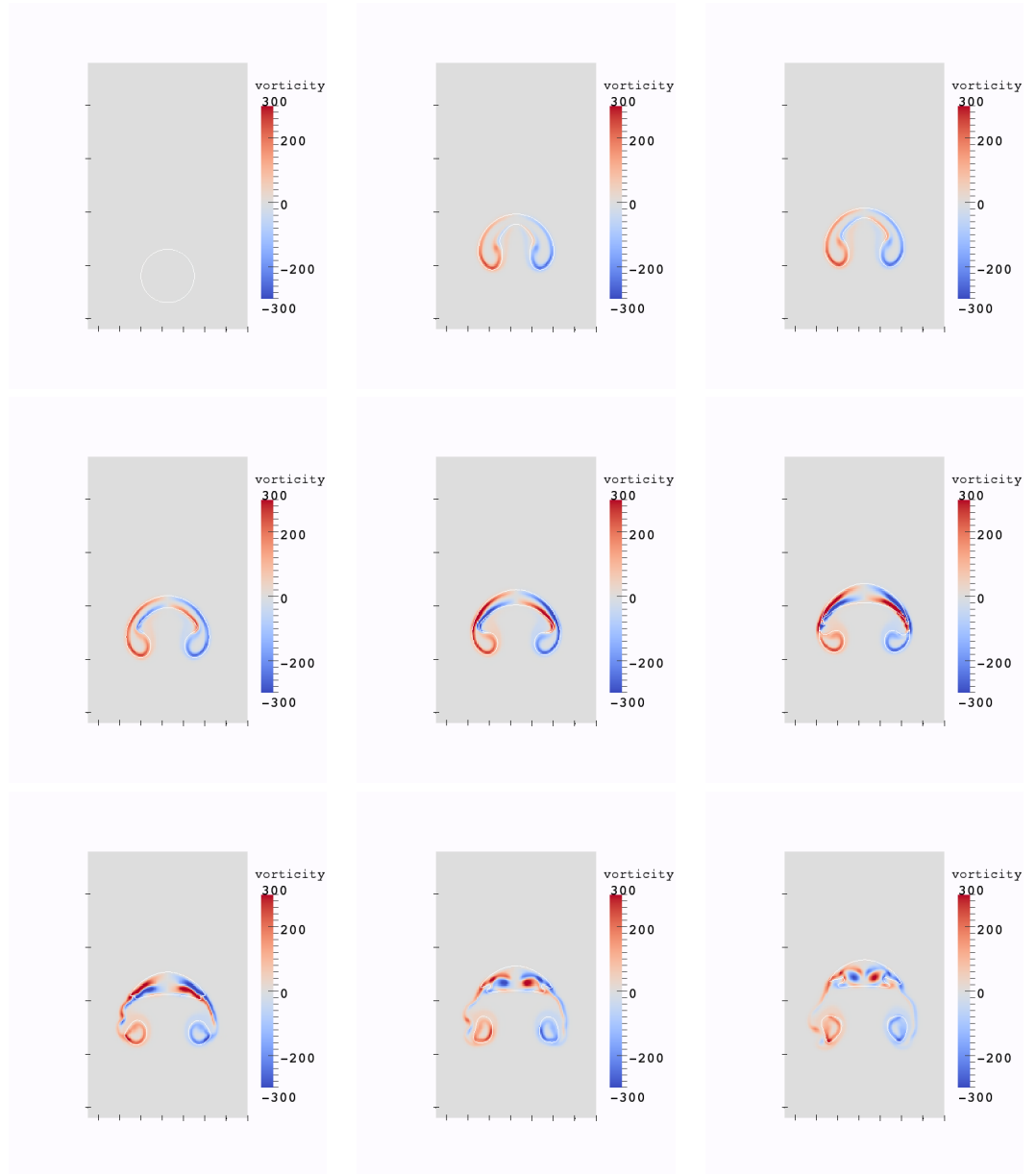


Figure 11. Evolution of the interface and vorticity values for the bubble test case from [36] at non-dimensional times $t * \sqrt{-g/0.025} = 0, 2.8, 6.4, 4.4, 4.8, 5.2, 5.6, 6.$, resolution 120×200 .

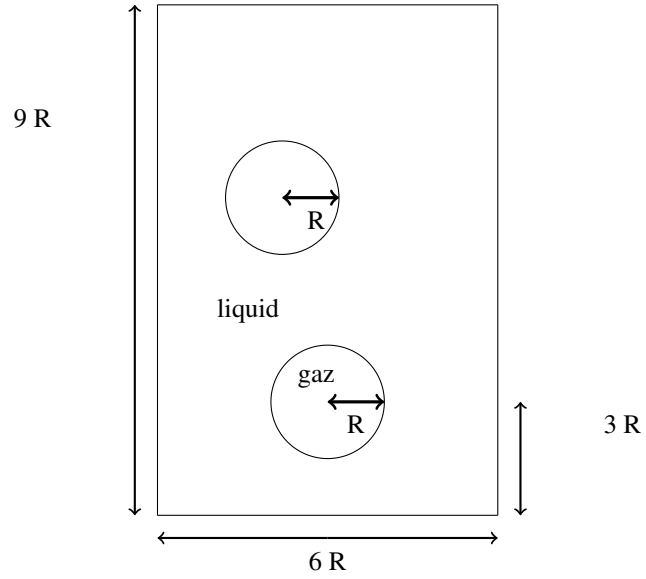


Figure 12. Initial fluid domain for the test case of the two rising bubbles in water

$$\left\{ \begin{array}{l} R = 0.025 \text{ m}, \\ \rho_{\text{water}} = 1000 \text{ kg/m}^3, \\ \mu_{\text{water}} = 1.137 \times 10^{-3} \text{ kg/ms}, \\ \rho_{\text{air}} = 1.226 \text{ kg/m}^3, \\ \mu_{\text{air}} = 1.78 \times 10^{-5} \text{ kg/ms}, \\ \sigma = 0.0728 \text{ kg/s}^2, \\ g = -9.8 \text{ m/s}^2. \end{array} \right. \quad (42)$$

415 The evolution of the interface and the vorticity values are plotted on Figure 11, for $120 \times$
416 200 grid points. We observe that the interface deforms in a way similar to the results in [36].

417 6.4. Two air bubbles in water

418 Two air bubble are initially at rest in water, see Figure 12. In the same time that they are
419 rising, their interaction produces larger deformations than for a single bubble. This test case is
420 meant to assessing the conservativity of the new method, as the increase in pression resolution is
421 meant to increase this conservativity.

422 The value of the physical parameters are

$$\left\{ \begin{array}{l} R = 1/30 \text{ m}, \\ \text{center of first bubble} = (0, 0), \\ \text{center of second bubble} = (-0.04, 0.08), \\ \text{final time } T_f = 0.12, \\ \rho_{\text{water}} = 1000 \text{ kg/m}^3, \\ \mu_{\text{water}} = 1.137 \times 10^{-3} \text{ kg/ms}, \\ \rho_{\text{air}} = 1.226 \text{ kg/m}^3, \\ \mu_{\text{air}} = 1.78 \times 10^{-5} \text{ kg/ms}, \\ \sigma = 0.0728 \text{ kg/s}^2, \\ g = -9.8 \text{ m/s}^2. \end{array} \right. \quad (43)$$

423 On Figure (13) are plotted the interface evolution and the vorticity values for the Ghost-Fluid
424 method (used for the pressure computation) and the new method. One observes small oscillations
425 of the vorticity near the interface between two fluids for the Ghost Fluid method, but not for the
426 new method. The conservation of the partial mass of air and momentum of air in each dimension
427 for the new method, and the Ghost-Fluid method are depicted respectively in Figure (14), Figure (
428 15) and Figure (16). Air being the less dense fluid, it is more prone to big oscillations if erroneous

429 mass and momentum transfers between the two fluids occur. One can observe that with the new
430 method and its second-order pressure resolution, the oscillations of these quantities are notably
431 less present than for the Ghost-Fluid. The partial mass is better conserved too.

432 7. Conclusions

433 We have developed a new method on Cartesian grids for the simulation of incompressible
434 flows with large density ratios. This method relies on a sharp resolution of the pressure term
435 across the interface defined by a level set function. The advantage of the proposed approach is its
436 simplicity to implement in an existing Cartesian mono-fluid Navier-Stokes solver as for instance
437 the Ghost-Fluid or CSF methods. It is only necessary to modify the stencil for the pressure
438 equation at some irregular grid points by adding one additional point. This Cartesian scheme uses
439 thus additional unknowns located on the interface to discretize with second-order accuracy the
440 jump conditions across the interface. The viscous term is treated with a regularizing approach
441 which allows to eliminate terms in the jump conditions. Indeed, it has been shown [32,33] that
442 the regularization has no significant impact on the accuracy of the results. Numerical results show
443 that this method leads to more accurate and stable results than some reference methods as for
444 instance the well known Ghost-Fluid or CSF methods. The conservation of volume of each phase
445 is also better conserved. We thus take advantage of both the regularity of the interface defined by
446 the level set function (curvature is numerically consistent), and the mass conservation of each
447 phase. The CLSVOF [11] can also provide good mass conservation and precision of the interface
448 but with a more complex numerical implementation.

449 Future works include an extension of the method to three-dimensional problems with
450 interactions with solids including the numerical simulation of wave energy converters [37,38].
451 We also aim to study the sensibility of the reinitialization procedure of the level set function
452 defining the bi-fluid interface, as for instance the one developed in [31].

453 **Funding:** This study has been carried out with financial support from the French State, managed by the
454 French National Research Agency (ANR) in the frame of the Investments for the future Programme IdEx
455 Bordeaux (ANR-10-IDEX-03-02)

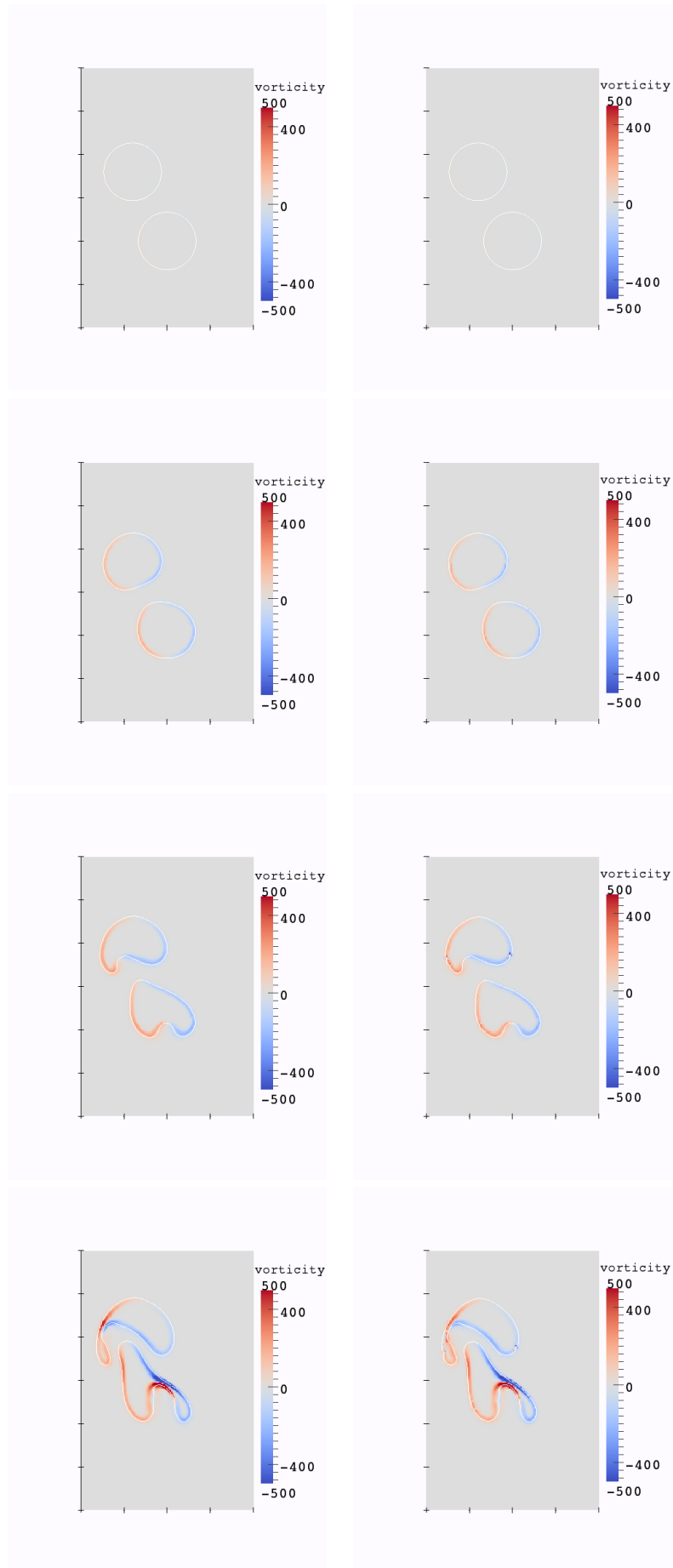


Figure 13. Evolution of the interface and vorticity values for the two bubbles test case at times $t = 0, 0.04, 0.08, 0.12$, resolution 120×180 , left: new method for pressure, right: Ghost-Fluid method for pressure.

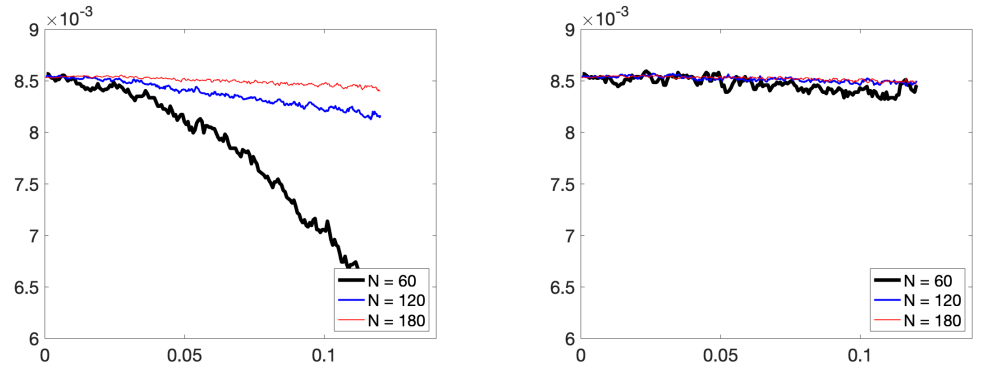


Figure 14. Evolution in time of partial mass of air with $N = 60, 90, 120$ points in x -direction with a) Ghost Fluid method, b) New method.

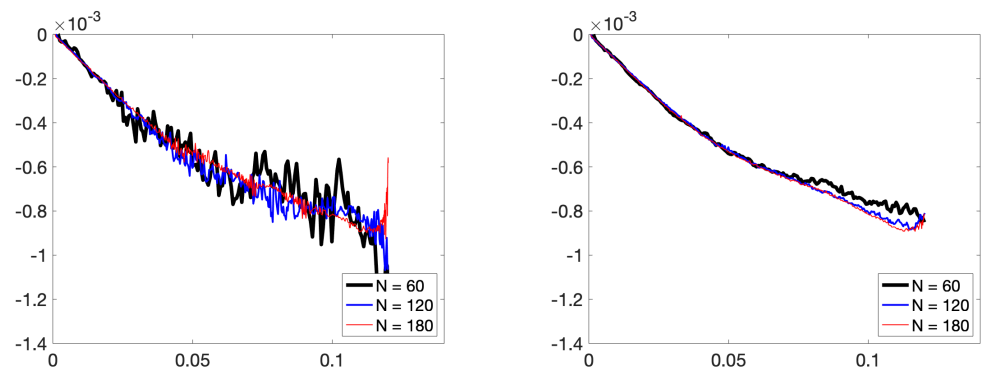


Figure 15. Evolution in time of partial x -momentum of air $N = 60, 90, 120$ points in x -direction with a) Ghost Fluid method, b) New method.

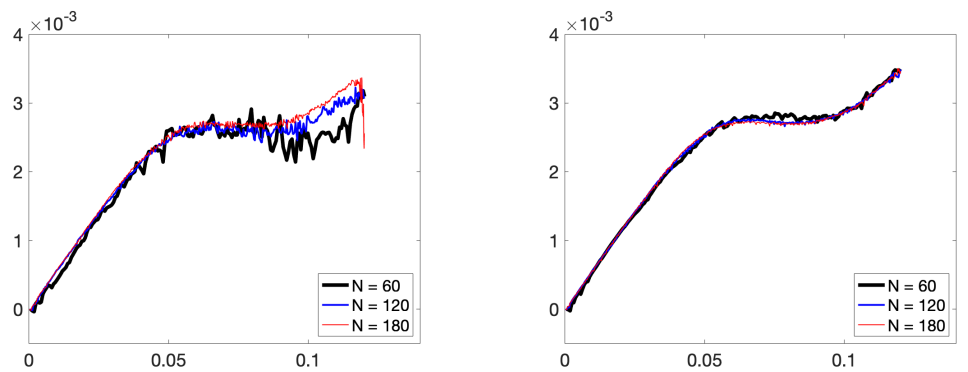


Figure 16. Evolution in time of partial y -momentum of air $N = 60, 90, 120$ points in x -direction with a) Ghost Fluid method, b) New method.

References

1. Cisternino, M.; Weynans, L. A parallel second order Cartesian method for elliptic interface problems. *Commun. Comput. Phys.* **2012**, *12*, 1562–1587.
2. Raessi, M.; Pitsch, H. Consistent mass and momentum transport for simulating incompressible interfacial flows with large density ratios using the level set method. *Computers and Fluids* **2012**, *63*, 70–81.
3. Brackbill, J.U.; Kothe, D.B.; Zemach, C. A continuum method for modeling surface tension. *J. Comput. Phys.* **1992**, *100*, 335–354.
4. M. Sussman, M.S.; Osher, S. A level-set approach for computing solutions to incompressible two-phase flows. *J. Comput. Phys.* **1994**, *114*, 146–159.
5. Galusinski, C.; Vigneaux, P. On stability condition for bifluid flows with surface tension: Application to microfluidics. *J. Comput. Phys.* **2008**, *227*, 6140–6164.
6. Kang, M.; Fedkiw, R.P.; Liu, X.D. A Boundary Condition Capturing Method for Multiphase Incompressible Flow. *Journal of Scientific Computing* **2000**, *15*, 323–360. doi:10.1023/A:1011178417620.
7. Liu, X.D.; Fedkiw, R.P.; Kang, M. A boundary capturing method for Poisson’s equation on irregular domains. *J. Comput. Phys.* **2000**, *160*, 151–178.
8. Couderc, F. Développement d’un code de calcul pour la simulation d’écoulements de fluides non miscibles: application à la désintégration assistée d’un jet liquide par un courant gazeux. PhD thesis, ENSAE, Toulouse, 2007.
9. Tanguy, S.; Menard, T.; Berlemont, A. A Level Set Method for vaporizing two-phase flows. *J. Comput. Phys.* **2007**, *221*, 837–853.
10. Rudman, M. A volume-tracking method for computing incompressible multifluid flows with large density variations. *Int. J. Numer. Meth. Fluids* **1998**, *28*, 357–378.
11. Sussman, M.; Puckett, E.G. A coupled level set and volume of fluid method for computing 3D and axisymmetric incompressible two-phase flows. *J. Comput. Phys.* **2000**, *162*, 301–337.
12. Sussman, M.; Smith, K.M.; Hussaini, M.Y.; Ohta, M.; Zhi-Wei, R. A sharp interface method for incompressible two-phase flows. *J. Comput. Phys.* **2007**, *221*, 469–505.
13. Hu, X.; Khoo, B.C.; Adams, N.A.; Huang, F.L. A conservative interface method for compressible flows. *J. Comput. Phys.* **2006**, *219*, 553–578.
14. Nangia, N.; Griffith, B.E.; Patankar, N.A.; Bhalla, A.P.S. A robust incompressible Navier-Stokes solver for high density ratio multiphase flows. *Journal of Computational Physics* **2019**, *390*, 548–594. doi:https://doi.org/10.1016/j.jcp.2019.03.042.
15. Nangia, N.; Patankar, N.A.; Bhalla, A.P.S. A DLM immersed boundary method based wave-structure interaction solver for high density ratio multiphase flows. *Journal of Computational Physics* **2019**, *398*, 108804. doi:https://doi.org/10.1016/j.jcp.2019.07.004.
16. Osher, S.; Sethian, J.A. Fronts propagating with curvature-dependent speed: Algorithms based on Hamiltonâ Jacobi formulations. *J. Comput. Phys.* **1988**, *79*.
17. Sethian, J.A. *Level Set Methods and Fast Marching Methods*; Cambridge University Press, Cambridge, UK, 1999.
18. Sethian, J.A. Evolution, Implementation, and Application of Level Set and Fast Marching Methods for Advancing Fronts. *J. Comput. Phys.* **2001**, *169*, 503–555.
19. Osher, S.; Fedkiw, R. *Level Set Methods and Dynamic Implicit Surfaces*; Springer, 2003.
20. Adalsteinnsson, D.; Sethian, J.A. The Fast Construction of Extension Velocities in Level Set Methods. *J. Comput. Phys.* **1999**, *148*, 2–22.
21. Rhie, C.; Chow, W. Numerical study of the turbulent flow past an airfoil with trailing edge separation. *AIAA Journal* **1983**, *21*, 1525–1532.
22. Mittal, R.; Dong, H.; Bozkurtas, M.; Najjar, F.; Vargas, A.; von Loebbecke, A. A versatile sharp interface immersed boundary method for incompressible flows with complex boundaries. *Journal of Computational Physics* **2008**, *227*, 4825 – 4852.
23. Chorin, A. Numerical solution of the Navier-Stokes equations. *Math. Comp.* **1968**, *22*, 745–762.
24. Temam, R. Sur l’approximation de la solution des equations de Navier-Stokes par la méthode des pas fractionnaires II. *Archiv. Rat. Mech. Anal.* **1969**, *32*, 377–385.
25. Sethian, J. A fast marching level set method for monotonically advancing fronts. *Applied Mathematics* **1996**, *93*, 1591–1595.
26. Rouy, E.; Tourin, A. A viscosity solutions approach to shape-from-shading. *SIAM J. Numer. Anal.* **1992**, *29*, 867–884.
27. Y.-H.; Cheng, L.T.; Osher, S.; Zhao, H.K. Fast sweeping algorithms for a class of Hamilton-Jacobi equations. *SIAM J. Numer. Anal.* **2003**, *41*, 673–694.
28. shan Jiang, G.; Shu, C.W.; L, I. Efficient Implementation of Weighted ENO Schemes. *J. Comput. Phys* **1995**, *126*, 202–228.
29. Russo, G.; Smereka, P. A remark on computing distance functions. *J. Comput. Phys.* **2000**, *163*, 51–67.
30. duChene, A.; Min, C.; Gibou, F. Second-order accurate computation of curvatures in a level set framework using novel high-order reinitialization schemes. *J. Sci. Comput.* **2008**, *35*, 114–131.
31. Luddens, F.; Bergmann, M.; Weynans, L. Enablers for high-order level set methods in fluid mechanics. *Int. J. Numer. Meth. Fluids* **2015**, *79*, 654–675.
32. Desjardins, O.; Pitsch, H. A spectrally refined interface approach for simulating multiphase flows. *J. Comput. Phys.* **2009**, *228*, 1658–1677.
33. Herrmann, M. The influence of density ratio on the primary atomization of a turbulent jet in crossflow. *Proc. Combust. Inst.* **2011**, *33*, 2079–2088.
34. Chenadec, V.L.; Pitsch, H. A monotonicity preserving conservative sharp interface flow solver for high density ratio two-phase flows. *J. Comput. Phys.* **2013**, *249*, 185–203.
35. Martin, J.C.; Moyce, W.J. An experimental study of the collapse of liquid columns on a rigid horizontal plane. *Philos. Trans. R. Soc. London, Ser. A* **1952**, *244*, 312–324.

-
36. Grenier, N.; Antuono, M.; Colagrossi, A.; Touze, D.L.; Alessandrini, B. An Hamiltonian interface SPH formulation for multi-fluid and free-surface flows. *J. Comput. Phys.* **2009**, *228*, 8380–8393.
 37. Khedkar, K.; Nangia, N.; Thirumalaisamy, R.; Bhalla, A.P.S. The inertial sea wave energy converter (ISWEC) technology: Device-physics, multiphase modeling and simulations. *Ocean Engineering* **2021**, *229*, 108879. doi:<https://doi.org/10.1016/j.oceaneng.2021.108879>.
 38. Bhalla, A.P.S.; Nangia, N.; Dafnakis, P.; Bracco, G.; Mattiazzo, G. Simulating water-entry/exit problems using Eulerian–Lagrangian and fully-Eulerian fictitious domain methods within the open-source IBAMR library. *Applied Ocean Research* **2020**, *94*, 101932. doi:<https://doi.org/10.1016/j.apor.2019.101932>.